Mechanical Characterization of an Additively Manufactured Inconel 718 Theta-Shaped Specimen

ERCAN CAKMAK, THOMAS R. WATKINS, JEFFREY R. BUNN, RYAN C. COOPER, PARIS A. CORNWELL, YANLI WANG, LINDSAY M. SOCHALSKI-KOLBUS, RYAN R. DEHOFF, and SUDARSANAM S. BABU

Two sets of "theta"-shaped specimens were additively manufactured with Inconel 718 powders using an electron beam melting technique with two distinct scan strategies. Light optical microscopy, mechanical testing coupled with a digital image correlation (DIC) technique, finite element modeling, and neutron diffraction with *in situ* loading characterizations were conducted. The cross-members of the specimens were the focus. Light optical micrographs revealed that different microstructures were formed with different scan strategies. *Ex situ* mechanical testing revealed each build to be stable under load until ductility was observed on the cross-members before failure. The elastic moduli were determined by forming a correlation between the elastic tensile stresses determined from FEM, and the elastic strains obtained from DIC. The lattice strains were mapped with neutron diffraction during *in situ* elastic loading; and a good correlation between the average axial lattice strains on the cross-member and those determined from the DIC analysis was found. The spatially resolved stresses in the elastic deformation regime are derived from the lattice strains and increased with applied load, showing a consistent distribution along the cross-member.

DOI: 10.1007/s11661-015-3186-8
© The Minerals, Metals & Materials Society and ASM International (outside the USA) 2015

I. INTRODUCTION

ADDITIVE manufacturing (AM) techniques enable the manufacture of engineering components layer-by-layer from raw feedstock materials such as powders, wires/rods, and tapes.[1–4] Over the past decade, AM techniques have been advanced to the point that some predict a 'renaissance in manufacturing'[5] which will enable the manufacturing of specialized high-value, high-performance products. The underlying idea of these novel techniques is to be able to manufacture fully functional complex structures housing embedded/enclosed features, which are either not possible or too expensive to obtain with subtractive manufacturing. The widespread application of such techniques can potentially revolutionize the way many engineering components are made today; eliminating the need for legacy tooling, extensive part inventories, long lead times; and minimizing waste generation.

Currently, the AM processes are more suited for relatively high-value alloys such as the Ti-6Al-4V[6–9] and nickel-base superalloys,[10–19] mainly due to the substantial financial benefit of reduced material waste and minimized machining processes, both associated with conventional subtractive manufacturing techniques. For instance, Dehoff *et al.*[9] has reported reducing the "buy to fly" ratio from 33:1 to nearly 1:1 for a Ti-6Al-4V bleed air leak detect bracket used in aircraft when manufactured with AM. Among the nickel-base superalloys, Inconel 718 (IN718) is known as a 'work-horse' alloy[20] especially for critical aero-engine and space applications. IN718 is an fcc γ matrix precipitation-strengthened alloy with the primary strengthening bct γ'' phase (Ni_3Nb, $D0_{22}$); and it

ERCAN CAKMAK and RYAN C. COOPER, Postdoctoral Research Associates, THOMAS R. WATKINS and RYAN R. DEHOFF, Senior Research Staffs, and YANLI WANG, Research Staff, are with the Materials Science and Technology Division, Oak Ridge National Laboratory, Oak Ridge, TN 37831-6064. Contact e-mail: cakmake@ornl.gov JEFFREY R. BUNN and LINDSAY M. SOCHALSKI-KOLBUS, Postdoctoral Research Associates, are with the Chemical and Engineering Materials Division, Oak Ridge National Laboratory. PARIS A. CORNWELL, Scientific Associate, is with the Instrument and Source Division, Oak Ridge National Laboratory. SUDARSANAM S. BABU, Governor's Chair, is with the Department of Materials Science and Engineering, The University of Tennessee, Knoxville, TN 37996, and also with the Energy & Transportation Science Division, Oak Ridge National Laboratory, also with the Department of Mechanical, Aerospace and Biomedical Engineering, The University of Tennessee.
Manuscript submitted July 3, 2015.

This manuscript has been authored by UT-Battelle, LLC under Contract No. DE-AC05-00OR22725 with the U.S. Department of Energy. The United States Government retains and the publisher, by accepting the article for publication, acknowledges that the United States Government retains a nonexclusive, paid-up, irrevocable, worldwide license to publish or reproduce the published form of this manuscript, or allow others to do so, for United States Government purposes. The Department of Energy will provide public access to these results of federally sponsored research in accordance with the DOE Public Access Plan (http://energy.gov/downloads/doe-public-access-plan).

Published online: 20 November 2015

possesses excellent high temperature strength, creep resistance, and corrosion/oxidation resistance.[11,13,17,21]

Particularly, the powder-based AM technologies have gathered significant attention[1,3,8,9,12–18, 22,23] wherein a fine layer of the metal powder (typically ~50 to 100 μm thick) is raked on the build table and a heat source such as an electron[1,8,9,14,16,22] or laser beam[12,13,15,17,18] first preheats the powder and then fuses it by melting the material locally in a pattern. This sequence continues on a build elevator which incrementally lowers the build piece down by an amount equal to the height of the last fused layer.[24,25]

A majority of the previous research of AM materials has utilized conventional mechanical characterizations, such as tension, compression, and flexure,[16] with standard shaped test samples, either as-built or extracted out of the as-built blocks.[13,15] Further, much of AM-reported work involved simpler geometries such as rectangular or cylindrical blocks as well as thin-walled shapes.[8,11,13–15,18,19,22,26] While such studies are necessary for a fundamental understanding of these processes, many real world engineering components are not in the form of simple shapes. Therefore, testing of more complex structures is crucial for progression to a more mature understanding of value and limitations of AM techniques and future development strategies for the uptake of these technologies.

In this study, IN718 theta-shaped specimens[27,28] (see Figure 1), named after the physical resemblance to the Greek letter "θ", were additively manufactured, as a model complex geometry, using electron beam melting. Such samples better represent engineering structures both in complexity of design (with arches and interconnecting beams such as in support structures) and the character of load distributions, *e.g.*, enforcing built-in constraints particularly to the cross-member. Furthermore, two sets of distinct build/scan strategies were employed to investigate their influence on the as-built microstructures and mechanical behavior. Light optical micrographs are presented to show the as-built microstructures of each build. *Ex* and *in situ* mechanical testing was conducted with primary emphasis on the cross-member. In this context, *ex situ* mechanical testing was coupled with digital image correlation (DIC) technique to obtain the distribution of strains on the loaded structure. Finite Element Modeling (FEM) was used to estimate the macroscopic stresses experienced by the cross-member during elastic deformation. Finally, spatially resolved strain/stress mapping was performed along the cross-member using neutron diffraction during *in situ* elastic mechanical loading.

II. EXPERIMENTAL DETAILS

A. *Sample Fabrication with EBM*

Two sets of five IN718 theta-shaped specimens were built using the Arcam EBM technique at ORNL's Manufacturing Demonstration Facility (MDF) with an Arcam S12 machine. The rotary atomized powder had the composition of 18.2 pct Fe, 18.2 pct Cr, 3 pct Mo, 5 pct Nb, 1 pct Ti, 0.5 pct Al, 0.1 pct Co, 0.1 pct Mn, 0.05 pct Cu, 0.2 pct Si, 0.05 pct C(max), and balance Ni, in wt pct. The size distribution of the powder particles was in the range of 40 to 125 μm. The build plate was preheated to a temperature of 1248 K (975 °C) and held for 30 minutes to allow the temperature to stabilize throughout the powder bed. A layer thickness of 50 μm was used for the build. One set of specimens was built with a beam scan pattern that manipulated the electron beam to result in a point heat source, *i.e.*, spot source. The second set of specimens was built using Arcam's standard commercially available melt theme for IN718 that treats the electron beam as a line source. The schematics illustrating the build sequences for both the Spot and Line Builds are presented in Figures 2(a) and (b), respectively. The Spot Build theme consists of melting the powder one 'spot' at a time in a pattern. The Line Build theme on the other hand, consists of a snake-like raster pattern that is rotated 90 deg after each layer.

Next, Figure 3 shows (a) comprehensive report of measured pressure within the column, chamber, and

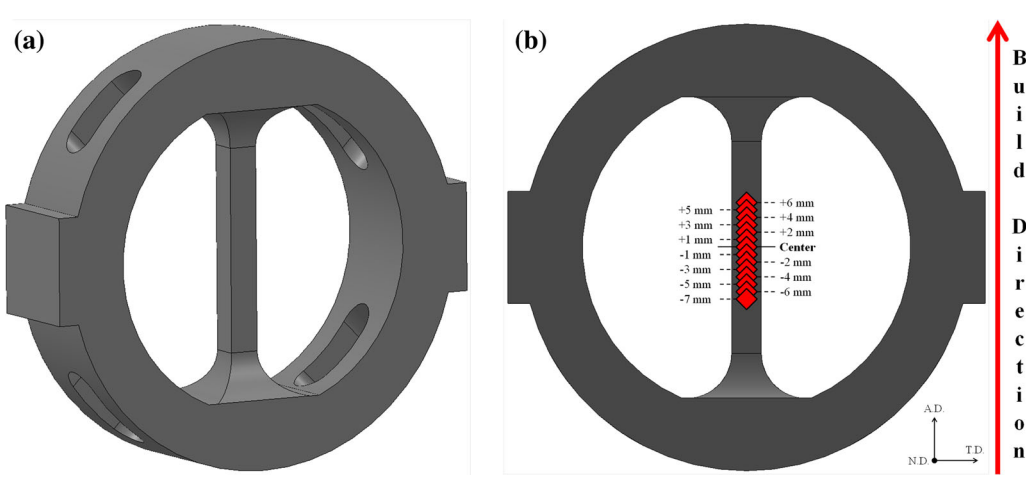

Fig. 1—(*a*) A 3D drawing of the theta specimen used in this work and (*b*) the location of the neutron diffraction mapping points along the cross-member. A.D., T.D., and N.D. refer to the axial, transverse, and normal directions, respectively.

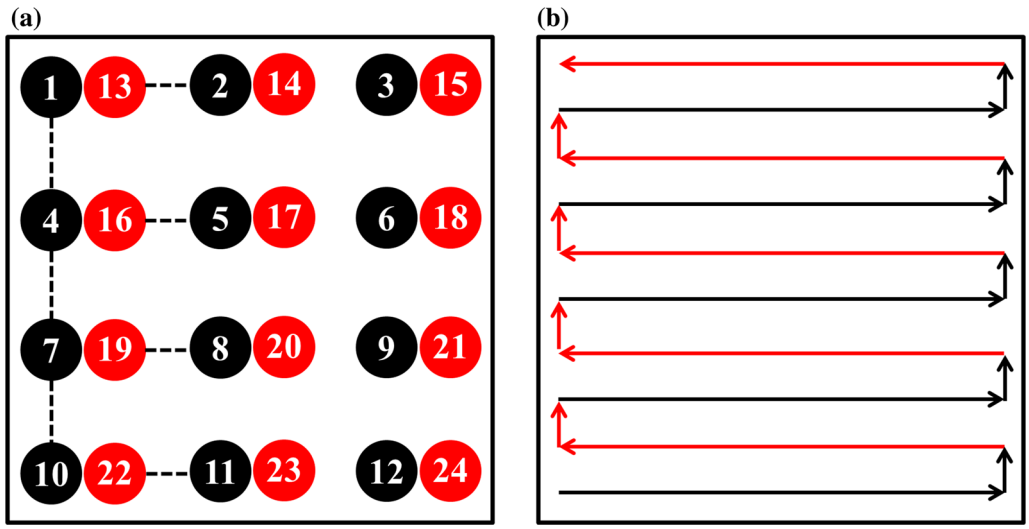

Fig. 2—Schematics illustrating the build patterns of the (*a*) Spot and (*b*) Line build strategies.

backing pumps, rake position, electron beam current, backing plate temperature, and also the layer height, as well as, (b) variation of electron beam current for the Spot and Line Build regions during one layer. The plots show unique characteristics of the electron beam currents changing rapidly during the build. The scanning speed during the processing is defined by the instrument software which is a function of the electron beam current and the geometry of the build defined. While the "speed function parameter" is given, the speed is not. However, the scan speeds may range from 800 to 4530 mm/s.[29] The details of the algorithms and instrument details are outlined in a series of patents published by Arcam AB.[30] Additionally, the beam power can be calculated by multiplying the accelerating voltage (60 keV) and the currents (see Figure 3).

Throughout the building process, the temperature stabilized at 1273 K (1000 °C). Additionally, the chamber and column pressures remained stable throughout the build process, with fluctuations in the chamber pressure being within normal variance during the melting process. Overall, the average layer time was 70 seconds. The building of the samples took 24 hours followed by a cooling stage of 7.2 hours. The build was allowed to cool under vacuum conditions. After the completion of the build, the parts were separated from the plate using electric discharge machining (EDM). No additional heat treatments were performed on the samples.

The build direction was parallel to the long axis of the cross-member (see axial direction in Figure 1(b)). In order to obtain the axial strain components from the cross-member during the *in situ* neutron diffraction experiments, these theta-shaped specimens were designed housing four beam windows (see Figure 1(a)), two of which are necessary to enable uninterrupted access of the incident beam to the cross-member and the diffracted beams to the detectors; and the other two to induce a symmetric distribution of load. Additionally, flat loading regions were built onto the theta specimens for easier alignment of the samples between the compression platens and to prohibit sample slip during loading (see Figure 1, at the 9 and 3 o'clock positions). The surfaces of these loading regions were machined flat and checked for parallelism before actual loading. The cross-member was designed to have a 4×4 mm^2 area with a total length of 40.4 mm and gage length of 28.4 mm. The samples had outer and inner ring diameters of 60 and 44 mm, respectively. The beam windows were 9 mm long and 6 mm wide, and the ring thickness was 15 mm to accommodate the beam windows. The samples were designed to initiate the failure in the cross-member.

B. *Ex situ Mechanical Testing*

The loading scheme of the theta specimen involves the application of compressive forces on the flat loading regions (Figure 1) which translate into a tensile stress along the cross-member. In order to obtain the macroscopic deformation response, one of the theta samples from each build was loaded *ex situ* under compression, using an electromechanical uniaxial load frame with a cross-head displacement rate of 5×10^{-3} mm/s, until failure of the cross-member. The samples were coated with a speckle-pattern, and the DIC technique was used to obtain the distribution of the strains on the cross-member and the ring of the samples during the loading/deformation. The Correlated Solutions VIC-3D™* image analysis software was used for the processing of DIC data.

*Correlated Solutions VIC-3D™ ⊗image analysis software, Correlated Solutions, Inc., Columbia, SC, USA, 2010.

C. *Neutron Diffraction Measurements*

In situ loading-neutron diffraction measurements were performed at the Second Generation Neutron Residual Stress Mapping Facility (NRSF2), beamline HB-2B, at the High Flux Isotope Reactor (HFIR), ORNL. A monochromatic wavelength of 1.53917 Å was

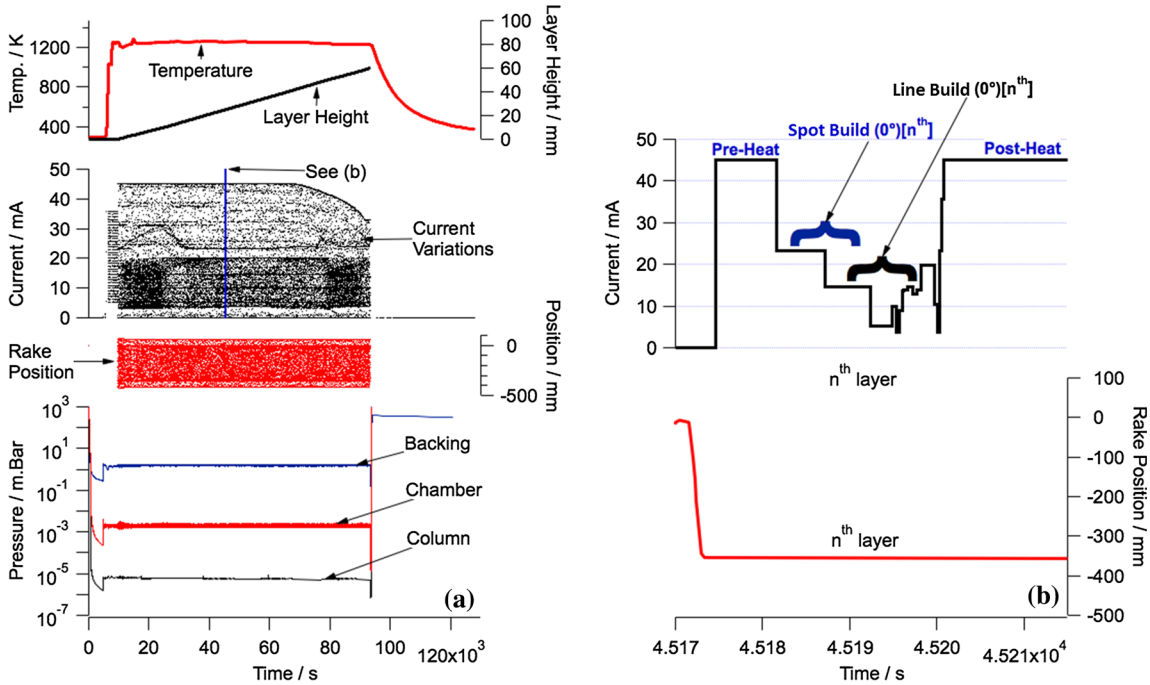

Fig. 3—Theta specimen build EBM process information (*a*) Temperature and pressure variation throughout the build process and (*b*) Representative electron beam current profile for a single layer.

obtained using the (422) planes of a Si monochromator. The detector was set at a 2θ angle of ~90 deg to detect the (311) reflection of the γ phase, which also allowed us to obtain a cubic gage volume inside the scanned area. A gage volume of $2 \times 2 \times 2$ mm^3 was defined for these measurements to ensure full burial of the beam inside the cross-member and obtain good counting statistics. Mapping along the cross-member was performed at 14 points, each 1 mm apart (−7 mm to +6 mm from the center), as shown in Figure 1(b). The measurements were performed for two sample directions, *i.e.*, axial/build and the normal directions (see Figure 1(b)). The *in situ* loading setup is presented in Figure 4 with the sample positioned to obtain the axial strain component; also showing the functionality of the beam windows.

D. *Finite Element Modeling*

A static analysis was performed using the ABAQUS FEM[31] package with a tetrahedral mesh as shown in Figure 5 to determine the elastic tensile stresses experienced by the cross-member. The mesh was defined using Tetgen's 10-node tetrahedral mesh generation.[32] A mesh sensitivity study was performed for the FEM analyses with 82,883 elements, 128,406 elements, and 301,717 elements. The solution was judged to be converged between the calculations, and the analysis was continued with 301,717 elements. The final mesh consisted of 301,717 tetrahedral 10-noded elements and 475,525 nodes. The material model assumed an isotropic, linear-elastic constitutive response. The ABAQUS nonlinear solver was implemented, but no nonlinearities developed within 1 mm displacement. This was considered the linear-elastic regime of interest. Figure 5 shows the coordinate system and boundary conditions. The boundary on the left-most flat was given a prescribed displacement in 150 to 300 μm increments up to 1 mm. The resultant load, F, was calculated as the sum of reaction forces on the nodes on this surface. The cross-member stress was calculated as the average axial stress in the y-direction, *i.e.,* σ_{yy}. The stress, σ_{yy}, as a function of the applied load, F, was determined to be solely dependent upon geometry. These results generated a measure of stress in the cross-member as a function of the applied load and geometry for the linear-elastic deformation regime in the absence of an analytical solution.

III. RESULTS AND DISCUSSION

A. *As-Built Specimens*

The as-built theta specimens still attached to the build plate are shown in Figure 6. Both sets of beam parameters are observed to produce structurally stable builds without any sign of cracking, warping (especially along the cross-member and around the beam windows), or de-bonding from the build plate. Additionally, the Line Build was found to produce a slightly smoother surface finish compared to the Spot Build.

One sample from each build was sectioned using EDM. The sectioned parts were then ground, polished, and examined using optical microscopy. The effective dimensions of both builds were taken just below the surface discontinuities, *i.e.*, beneath the rough as-built surface. Accordingly, the effective cross-member widths were measured to be 4.13 and 3.62 mm on average for the Spot and Line Builds, respectively. The effective ring thicknesses, on the other hand, were measured to be 14.7

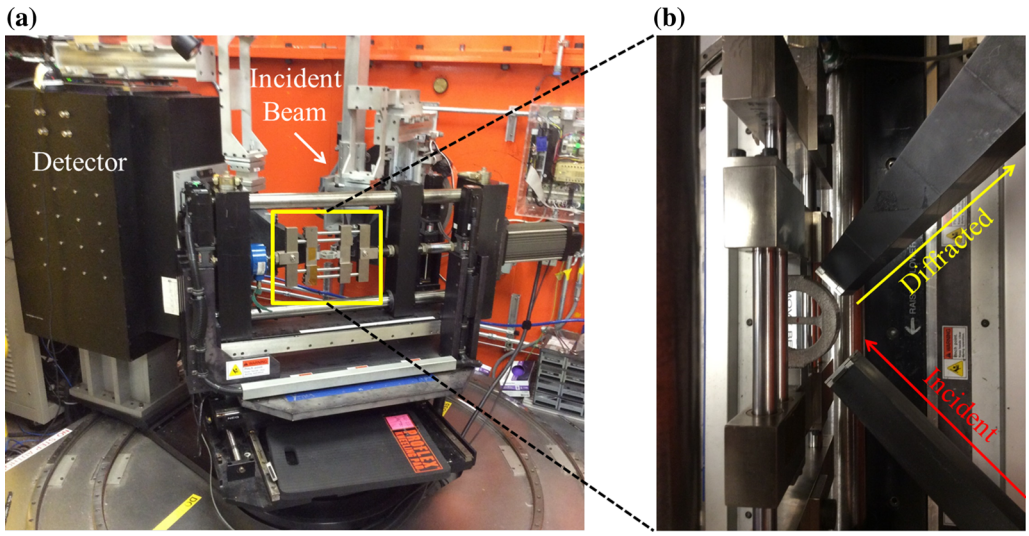

Fig. 4—(*a*) The *in situ* loading setup used at NRSF-2 (beamline HB-2B), HFIR, ORNL. (*b*) A close-up view from above of the theta specimen inside the compression fixture with the load frame positioned to obtain the axial strains along the cross-member. Note that the incident and diffracted beams pass through the beam windows of the specimen.

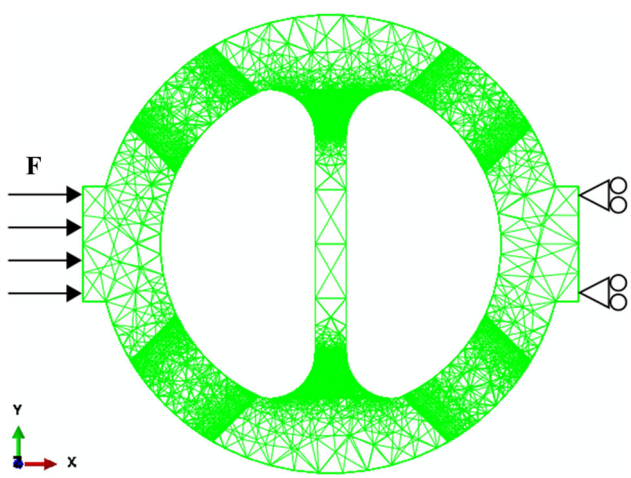

Fig. 5—The theta specimen mesh and the loading scheme used for FEM calculations, where F is the applied load. Notice that the nodes are more heavily concentrated around more complicated regions such as areas of curvature and the beam windows.

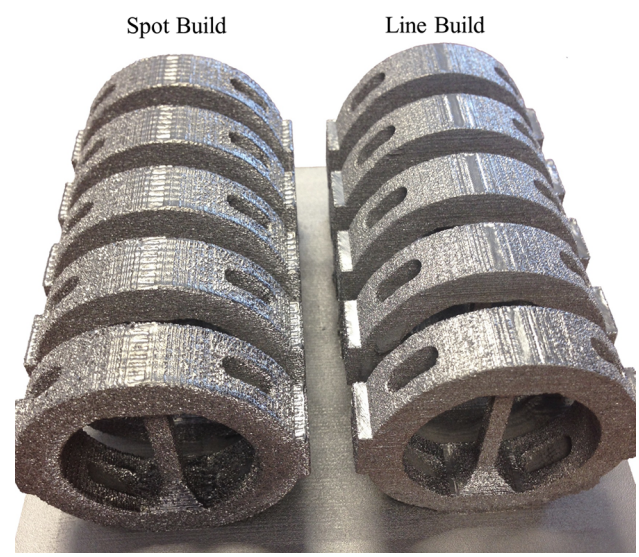

Fig. 6—The as-built theta specimens on the build plate; built with two different scan strategies: Spot Build (left) and Line Build (right).

and 14.23 mm for the Spot and Line Builds, respectively. The biggest differences between the as-seen and the effective dimensions were observed in the Spot Build due to its rougher surface finish.

Additionally, optical micrographs from the cross-members are presented in Figures 7(a) and (b) for the Spot and Line Builds, respectively. Due to the highly corrosion resistant nature of IN718, the samples were hard to etch. Nevertheless, in the micrographs certain features and differences between the builds are visible. Both samples show porosity in the as-built microstructures which is not uncommon in AM-built parts in their as-built states. Most importantly, distinct grain morphologies are observed in which the Spot Build is characterized with large columnar grains extending along the build direction while the Line Build shows a finer microstructure with "more close to" equiaxed shaped grains. However, further discussion of the microstructures remains out of the scope of this work and will be discussed in much greater detail in an upcoming publication.

B. *Ex Situ Mechanical Behavior*

The macroscopic mechanical behaviors of both builds are presented in Figure 8 in terms of applied cumulative loads *vs* the engineering strains experienced by the cross-members until they fail. The engineering strains on the cross-members are obtained from DIC, using a virtual extensometer. The theta-shaped samples were observed to be stable under load, and the cross-members were able to withstand a total

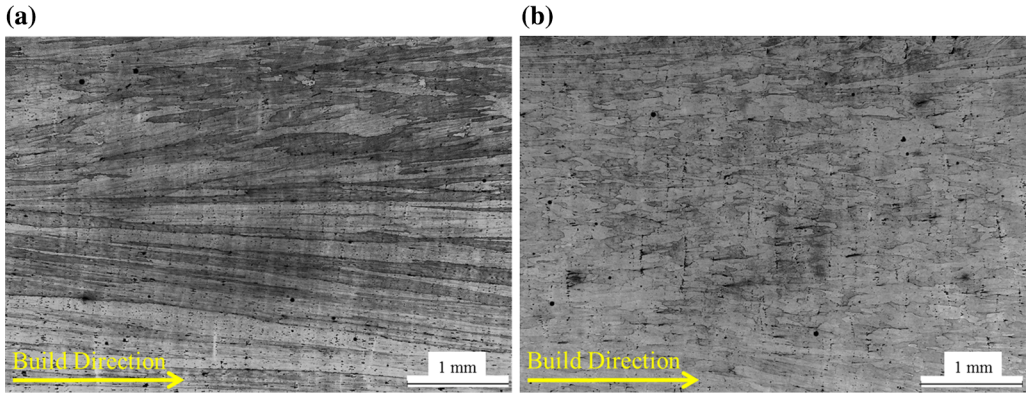

Fig. 7—Light optical micrographs obtained from the cross-members of (*a*) Spot Build and (*b*) Line Build along the build direction which is parallel to the horizontal axis of the images. The scale bar corresponds to 1 mm.

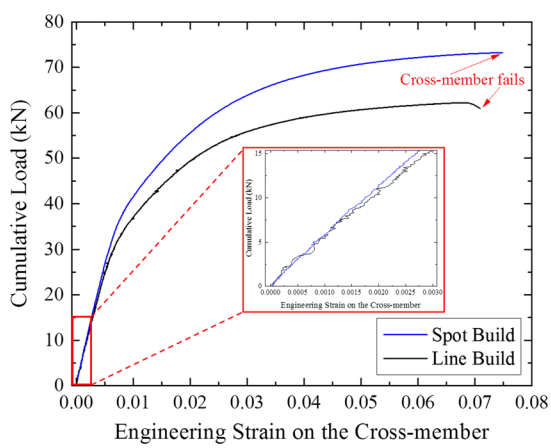

Fig. 8—The macroscopic deformation responses of the builds: the cumulative load as a function of the measured engineering strain on the cross-members of the theta specimens. In the inset is a close-up view of the elastic deformation zone studied with *in situ* neutron diffraction.

~7 to 7.5 pct engineering strain in tension before failure. No additional failure such as cracking occurred near the beam windows or other sections of the specimens.

The mechanical response at lower levels of applied loads (≤20 kN) is observed to be similar for both builds. However, the deformation curves start to deviate from each other as the cumulative load levels increase above ~25 kN; with the Spot Build bearing higher cumulative loads for a given strain increment on the cross-member. For the purposes of the current work, the emphasis is focused on the elastic deformation up to a total load of 15 kN. Although not discussed further here, a large portion of the differences in the two curves is expected to result from the fact that the ring and the cross-member dimensions of the Spot Build sample were slightly thicker.

In order to visualize the strain distributions, the major principle strains, ε_1, (determined from DIC) are presented in Figure 9 (in terms of Lagrange strains) as a function of position on the sample and applied engineering strain on the cross-member, from the Spot Build as an example. Figure 9 shows that as the load is increased the strain is maximum in the cross-member while the ring remains in a relatively low state of strain. Failure occurs on the cross-member first without the presence of heavy strain concentrations on other sections of the sample. The strain concentrations were found to be mainly sample geometry related and a similar strain distribution was observed in the Line Build (not presented here).

The static loading analysis with FEM was used to obtain the fraction of the cumulative load that is transferred to the cross-member as tensile stresses, in the elastic deformation regime. When plotted against the elastic strains obtained from DIC, this stress–strain relation (see Figure 10) reveals the elastic moduli to be ~162 and 168 GPa for the Spot and Line Builds, respectively; suggesting the Line Build to be slightly stiffer. This value is, however, well below the value of ~200 GPa reported for conventionally manufactured IN718 alloys.[33] This could, nevertheless, be expected since the specimens were tested in their as-built conditions without any precipitation hardening heat treatments. Lower values of elastic modulus in additively manufactured IN718 parts have also been previously reported by others.[34,35]

Additionally, although it will not be discussed further in this work, both builds are characterized with very strong (200) preferred orientations along the build directions with textures being slightly weaker in the case of the Line Build. A heavy presence of (200) (the most compliant planes for an FCC material) along the build/axial direction would support the lower modulus than the conventionally reported bulk value of 200 GPa. The elastic modulus of the (200) planes, E_{200}, of IN718 is reported to be 158 to 166 GPa.[36] Such results are found to agree with the bulk elastic moduli of 162 to 168 GPa obtained from the stress (FEM)–strain (DIC) response presented in this study. The preferred orientations are still part of ongoing investigation and will be presented in a future publication in detail.

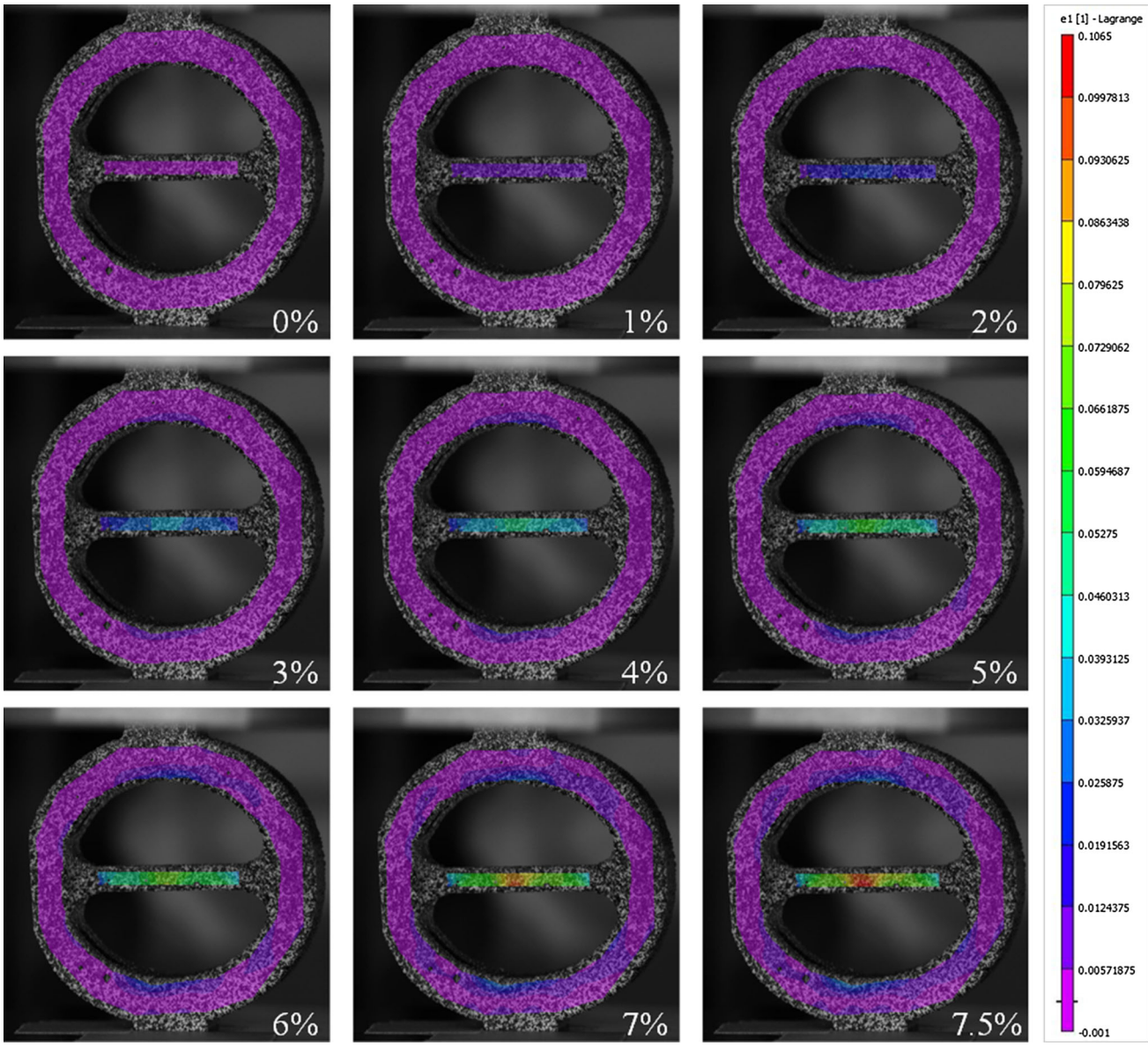

Fig. 9—The distribution of the principal strains (ε_1) on the cross-member and the ring of the theta specimens as a function of the applied macroscopic engineering strains (pct) experienced by the cross-member and obtained from the DIC analysis. Spot Build is presented as an example.

C. *Evolution of Lattice Strains During In Situ Loading*

The *in situ* loading experiments were performed in the elastic regime. An electromechanical load frame[37] with a maximum 20 kN load capacity was used to apply cumulative load levels of 0.4 (Holding Load), 3.7, 7.5, 11.2, and 15 kN, corresponding to macroscopic tensile strains of 0.0054 pct at the holding load and 0.272 pct at 15 kN on the cross-member, according to the load-strain correlation revealed by the DIC analysis. The lattice strains, ε_{hkl}, were calculated using Eq. [1][38] from the d-spacings, d^{hkl}, measured *in situ* with neutron diffraction

$$\varepsilon_{hkl} = \frac{d^{hkl} - d_0^{hkl}}{d_0^{hkl}}, \qquad [1]$$

where d_{hkl}^0 is the reference or stress-free interplanar spacing. In this work the strains are calculated with respect to the unloaded state (holding load), *i.e.*, the d_{hkl}^0 value corresponded to the *d*-spacing at the holding load. The (311) reflection was selected for the measurement of the strains as it is reported to be weakly affected by the intergranular strains for an FCC material.[38] These calculations were performed on a point-by-point basis for all the load levels, *i.e.*, for the mapping point of, *e.g.*, −3 mm at any load (see Figure 1), the d_0 value is taken from the same point (−3 mm in this case) at 0.4 kN load, *etc*. The mean axial and normal lattice strains (*i.e.*, averaged over the mapped area) in the cross-members are presented in Figure 11(a) as a function of applied cumulative load for both builds. A linear load–strain

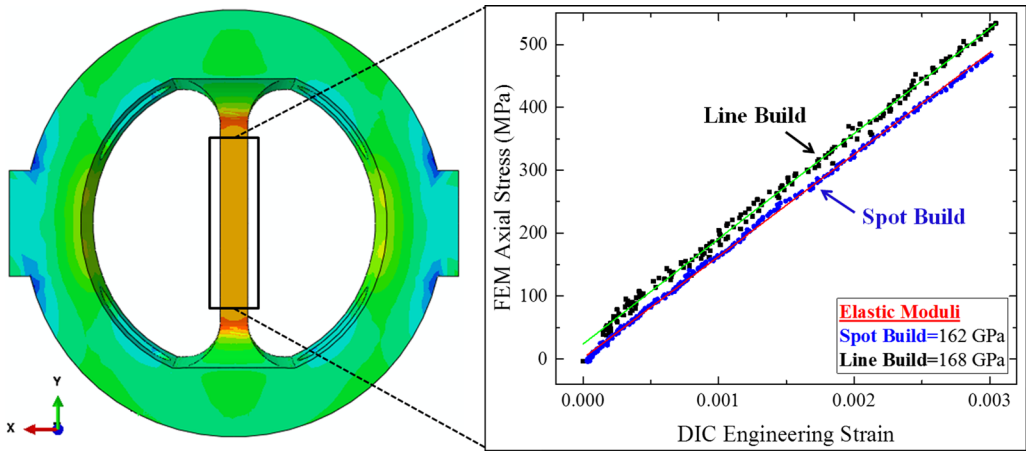

Fig. 10—The elastic axial stress (inferred from the Finite Element Modeling analysis) as a function of the elastic axial strain (obtained from the Digital Image Correlation technique) for the Spot and Line builds along the cross-members, revealing slopes of 162 and 168 GPa, respectively. No color bar is presented, as the loaded theta sample is presented for illustrative purposes only, showing that the data originate from the cross-member.

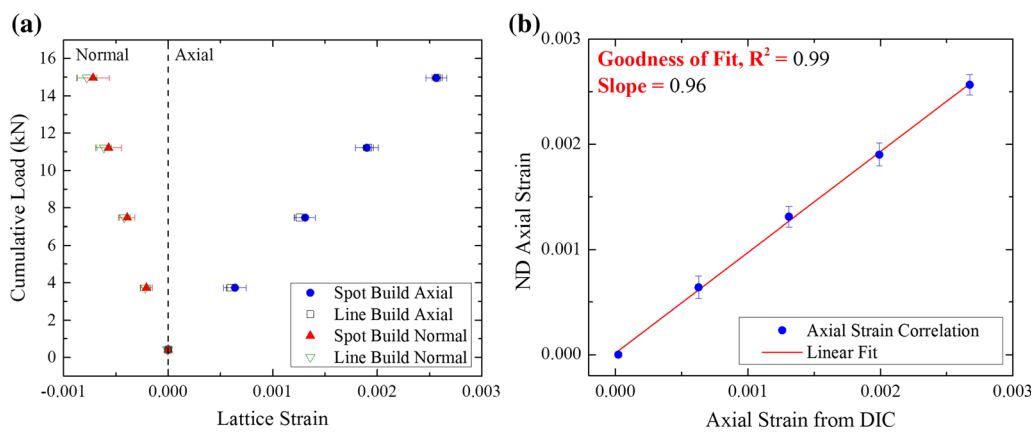

Fig. 11—(*a*) The evolution of the axial and normal lattice strains as a function of applied cumulative loads during *in situ* elastic loading measured with neutron diffraction; presented for both builds; (*b*) The correlation between the mean axial strains obtained from *in situ* neutron diffraction and the macroscopic axial strains obtained from the DIC analysis, acting along the cross-member. The neutron diffraction data points represent the averages of the 14 points mapped along the length of the cross-member, and the error-bars correspond to their standard deviation. The data from the Spot Build are presented as an example.

relation is observed where the data points from both builds show an almost perfect overlap. These results are also consistent with the macroscopic *ex situ* deformation response (see Figure 8), where both builds showed similar behavior up to the studied *in situ* load levels. Next in Figure 11(b), the correlation between the mean axial lattice strains obtained from neutron diffraction and the macrostrains obtained from the DIC analysis during *ex situ* deformation is presented for the Spot Build, as an example. The relation is observed to be linear and a very good fit with a slope of 0.96 (*i.e.*, showing a 96 pct agreement) is achieved. The slight discrepancy observed between the DIC and ND strains is expected considering that the rough surface finish of AM parts can influence DIC. The good agreement between the DIC and ND data also helps to verify that the use of the (311) reflection to estimate the bulk elastic response (for an FCC material) remains appropriate for the current work, for the studied load levels.

D. *Characterization of Stress Evolution During In Situ Loading*

The stresses for a given direction, σ_{ij}, were calculated using Eq. [2][38]

$$\sigma_{ij} = \frac{E_{\mathrm{hkl}}}{(1+\nu_{\mathrm{hkl}})}\left[\varepsilon_{\mathrm{ij}} + \frac{\nu_{\mathrm{hkl}}}{(1-2\nu_{\mathrm{hkl}})}\left(\varepsilon_{11}^{\mathrm{hkl}} + \varepsilon_{22}^{\mathrm{hkl}} + \varepsilon_{33}^{\mathrm{hkl}}\right)\right] \quad [2]$$

where E_{hkl} is the Young's Modulus, ν_{hkl} is the Poisson's Ratio, and ε_{ij} is the measured lattice strain in a given sample direction. Here, ε_{ii} are the principal strains. For the nomenclature of the current work, ε_{11} is taken as the loading/build/axial direction, ε_{22} as the normal, and ε_{33} as the transverse directions. Furthermore ε_{22} was regarded as equal to ε_{33}, per tensile deformation symmetry. This is an appropriate assumption as the loading is applied in known directions coincident with the sample geometry defined, and the stresses calculated are defined as only the stresses from an unloaded state.

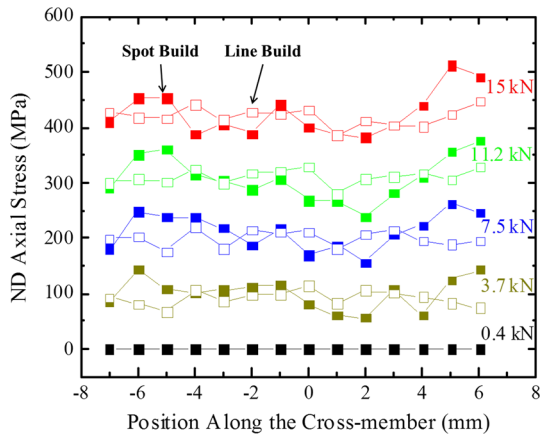

Fig. 12—The spatial distribution of the axial stresses along the cross-members of both builds, as determined using neutron diffraction from the theta specimens loaded *in situ*; presented for increasing levels of applied cumulative loads. As pointed with the arrows, closed and open symbols correspond to the Spot and Line Builds, respectively.

For the determination of stresses, ν was taken as 0.3 whereas E was obtained through the use of the FEM analysis (162 GPa for the Spot Build and 168 GPa for the Line Build). The distribution of the axial stresses calculated using Eq. [2] is presented in Figure 12 as a function of applied cumulative loads and mapping position on the cross-members of both builds. Figure 12 shows that with the increase of the applied load, the stresses along the build direction increase in tensile character, and a uniform load distribution is obtained along the cross-member for both builds.

Overall, both builds behaved as predicted within the elastic deformation regime. Even though such a conclusion may appear trivial for well-understood sample geometries and fabrication processes, it holds significant value for the maturation of AM techniques and their ability to build complex functional parts. By the same token, the successful build and testing of this model complex structure acts as a stepping stone toward achieving more complicated load-bearing structures with AM. This work also demonstrates the importance and versatility of neutron diffraction for nondestructive characterization of spatially resolved strains/stresses in a volume of material in fairly complex geometries, which most other characterization methods may fail to achieve.

IV. SUMMARY

In this work, complex theta-shaped specimens were additively manufactured from Inconel 718 powders using the electron beam melting technique. Two different build/scan strategies were used to obtain two sets of samples, *i.e.*, Spot and Line Builds. Both sets of samples were successfully built and mechanically tested to observe their stability under load. Light optical microscopy was used to observe the as-built microstructures. A DIC technique was used to obtain and visualize the strain distributions on the loaded structure, *ex situ*. FEM was used to estimate the loads transferred to the cross-member and to determine the elastic moduli of the builds in conjunction with strains determined from DIC. *In situ* neutron diffraction (ND) was used to map the distribution of strains/stresses along the cross-members during elastic loading.

Optical micrographs revealed distinct microstructures between the builds where the Spot Build mainly consisted of large columnar grains extending along the build direction while the Line Build showed a finer microstructure with the presence of "more close to" equiaxed shaped grains.

The *ex situ* mechanical testing revealed the samples of both builds to be stable under load with the cross-members withstanding ~7 to 7.5 pct engineering strain before failure. The samples failed on the cross-members without any additional failure on other parts of the specimens. Even though both builds showed similar macroscopic deformation behavior in the earlier levels of deformation (load ≤20 kN), deviations were observed starting with cumulative loads exceeding ~25 kN; with the Spot Build accumulating higher cumulative loads per strain increment on the cross-member mainly due to having slightly thicker ring and cross-member dimensions. A correlation between the elastic strains obtained from DIC and the elastic stresses obtained from FEM revealed elastic moduli of 162 and 168 GPa for the Spot and Line Builds, respectively.

In situ neutron diffraction (ND) was used to map the distribution of strains/stresses along the cross-members during elastic loading (cumulative load ≤15 kN). The mean axial lattice strains along the cross-member were found to show a very good agreement with the macroscopic elastic strains obtained from the DIC analysis. The *in situ* loading experiments further revealed the stresses experienced by the cross-members increase steadily in tensile character with increasing load levels as the theta samples were compressed. The spatial distributions of the microscopic stresses along the cross-members of both builds were found to be uniform for all the studied load levels.

ACKNOWLEDGMENTS

This research was sponsored by the Laboratory Directed Research and Development Program of Oak Ridge National Laboratory, managed by UT-Battelle, LLC, for the U. S. Department of Energy. Research at MDF was sponsored by the U.S. Department of Energy, Office of Energy Efficiency and Renewable Energy, Advanced Manufacturing Office, under contract DE-AC05-00OR22725 with UT-Battelle, LLC. Research at ORNL's High Flux Isotope Reactor was sponsored by the Scientific User Facilities Division, Office of Basic Energy Sciences, U.S. Department of Energy. EC and TRW would like to thank Dr. E. Andrew Payzant for the neutron beam time, Mr. Christopher O. Stevens for his help with the *ex situ* mechanical testing, and Mr. Tom Geer for optical mi-

croscopy measurements. Further, the authors gratefully acknowledge Dr. Donald L. Erdman III, Mr. Stephen Kulan, and Dr. Ke An for their timely help with the load frame during our measurements at HFIR. EC would also like to thank Dr. Michael M. Kirka for his valuable input and Mr. Cemal Kizildag for his assistance with image processing.

REFERENCES

1. C.A. Brice and W.H. Hofmeister: *Metall. Mater. Trans. A*, 2013, vol. 44A, pp. 5147–53.
2. R.R. Dehoff and S.S. Babu: *Acta Mater.*, 2010, vol. 58, pp. 4305–15.
3. W.J. Sames, K.A. Unocic, R.R. Dehoff, T. Lolla, and S.S. Babu: *J. Mater. Res.*, 2014, vol. 29, pp. 1920–30.
4. W.E. Frazier: *J. Mater. Eng. Perform.*, 2014, vol. 23, pp. 1917–28.
5. C.K. Chuma, K.F. Leong, and C.S. Lim: *Rapid Prototyping: Principles and Applications*, 2nd ed., World Scientific, Singapore, 2003.
6. S.S. Al-Bermani, M.L. Blackmore, W. Zhang, and I. Todd: *Metall. Mater. Trans. A*, 2010, vol. 41A, pp. 3422–34.
7. S.M. Gaytan, L.E. Murr, F. Medina, E. Martinez, M.I. Lopez, and R.B. Wicker: *Mater. Technol.*, 2009, vol. 24, pp. 180–90.
8. L.E. Murr, E.V. Esquivel, S.A. Quinones, S.M. Gaytan, M.I. Lopez, E.Y. Martinez, F. Medina, D.H. Hernandez, E. Martinez, J.L. Martinez, S.W. Stafford, D.K. Brown, T. Hoppe, W. Meyers, U. Lindhe, and R.B. Wicker: *Mater. Charact.*, 2009, vol. 60, pp. 96–105.
9. R. Dehoff, C. Duty, W. Peter, Y. Yamamoto, W. Chen, C. Blue, and C. Tallman: *Adv Mater Process*, 2013, vol. 171, pp. 19–22.
10. Y.C. Zhang, Z.G. Li, P.L. Nie, and Y.X. Wu: *Metall. Mater. Trans. A*, 2013, vol. 44A, pp. 708–16.
11. A. Strondl, S. Milenkovic, A. Schneider, U. Klement, and G. Frommeyer: *Adv. Eng. Mater.*, 2012, vol. 14, pp. 427–38.
12. T. Vilaro, C. Colin, J.D. Bartout, L. Naze, and M. Sennour: *Mater Sci Eng A-Struct*, 2012, vol. 534, pp. 446–51.
13. H. Qi, M. Azer, and A. Ritter: *Metall. Mater. Trans. A*, 2009, vol. 40A, pp. 2410–22.
14. A. Strondl, R. Fischer, G. Frommeyer, and A. Schneider: *Mater Sci Eng A-Struct*, 2008, vol. 480, pp. 138–47.
15. P.L. Blackwell: *J. Mater. Process. Technol.*, 2005, vol. 170, pp. 240–46.
16. A. Strondl, M. Palm, J. Gnauk, and G. Frommeyer: *Mater. Sci. Technol.*, 2011, vol. 27, pp. 876–83.
17. Y. Tian, D. McAllister, H. Colijn, M. Mills, D. Farson, M. Nordin, and S. Babu: *Metall. Mater. Trans. A*, 2014, vol. 45A, pp. 4470–82.
18. K.N. Amato, S.M. Gaytan, L.E. Murr, E. Martinez, P.W. Shindo, J. Hernandez, S. Collins, and F. Medina: *Acta Mater.*, 2012, vol. 60, pp. 2229–39.
19. K.N. Amato, J. Hernandez, L.E. Murr, E. Martinez, S.M. Gaytan, P.W. Shindo, and S. Collins: *J Mater Sci Res*, 2012, vol. 1, pp. 3–41.
20. C. Radhakrishna and K.P. Rao: *J. Mater. Sci.*, 1997, vol. 32, pp. 1977–84.
21. A. Devaux, L. Naze, R. Molins, A. Pineau, A. Organista, J.Y. Guedou, J.F. Uginet, and P. Heritier: *Mater Sci Eng A-Struct*, 2008, vol. 486, pp. 117–22.
22. L.E. Murr, E. Martinez, S.M. Gaytan, D.A. Ramirez, B.I. Machado, P.W. Shindo, J.L. Martinez, F. Medina, J. Wooten, D. Ciscel, U. Ackelid, and R.B. Wicker: *Metall. Mater. Trans. A*, 2011, vol. 42A, pp. 3491–08.
23. L. Sochalski-Kolbus, E. Payzant, P. Cornwell, T. Watkins, S. Babu, R. Dehoff, M. Lorenz, O. Ovchinnikova, and C. Duty: *Metall. Mater. Trans. A*, 2015, vol. 46A, pp. 1419–32.
24. L.E. Murr, S.M. Gaytan, D.A. Ramirez, E. Martinez, J. Hernandez, K.N. Amato, P.W. Shindo, F.R. Medina, and R.B. Wicker: *J. Mater. Sci. Technol.*, 2012, vol. 28, pp. 1–14.
25. D. Cormier, A. Harrysson, and H. West: *Rapid Prototyp. J.*, 2004, vol. 10, pp. 35–41.
26. P. Rangaswamy, M.L. Griffith, M.B. Prime, T.M. Holden, R.B. Rogge, J.M. Edwards, and R.J. Sebring: *Mater Sci Eng A-Struct*, 2005, vol. 399, pp. 72–83.
27. A.J. Durelli, S. Morse, and V. Parks: *Mater. Res Standard*, 1962, vol. 2, pp. 114–17.
28. G.D. Quinn: in *Fractography of Advanced Ceramics III*, J. Dusza, R. Danzer, R. Morrell, G.D. Quinn, eds., 2009, pp. 201–208.
29. R. Dehoff, M. Kirka, W. Sames, H. Bilheux, A. Tremsin, L. Lowe, and S. Babu: *Mater Sci Tech*, 2015, vol. 31, pp. 931–38.
30. M. Larsson: US Patent #US 7713454 B2, 11 May 2010.
31. ABAQUS: *ABAQUS Documentation*, Dassault Systèmes, Providence, RI, 2011.
32. H. Si: *ACM Trans. Math. Softw.*, 2015, vol. 41(2), art. no. 11.
33. Technical Bulletin: "Inconel Alloy 718", Special Metals Corporation, 2007.
34. B. Baufeld: *J. Mater. Eng. Perform.*, 2012, vol. 21, pp. 1416–21.
35. R.K. Bird and J. Hibberd: NASA Technical Memorandum Paper No. TM-2009-215929, 2009.
36. J. Repper, P. Link, M. Hofmann, C. Krempaszky, W. Petry, and E. Werner: *Appl Phys A-Mater*, 2010, vol. 99, pp. 565–69.
37. K. An, W.B. Bailey, S.O. Craig, H. Choo, C.R. Hubbard, and D.L. Erdman, III: *J J Neutron Res*, 2007, vol. 15, pp. 207–13.
38. M.T. Hutchings, P.J. Withers, T.M. Holden, and T. Lorentzen: *Introduction to the Characterization of Residual Stress by Neutron Diffraction*, Taylor and Francis, Boca Raton, FL, 2005.